Thermoelectric properties and high-temperature stability of the $Ti_{1-x}V_xCoSb_{1-x}Sn_x$ half-Heusler alloys

M. Asaad,[a] J. Buckman,[b] R. I. Smith[c] and J.W.G. Bos[a,*]

[a] *Institute of Chemical Sciences and Centre for Advanced Energy Storage and Recovery, School of Engineering and Physical Sciences, Heriot-Watt University, Edinburgh, EH14 4AS, UK.*

[b] *Institute of Petroleum Engineering, School of Energy, Geoscience, Infrastructure and Society, Heriot-Watt University, Edinburgh, EH14 4AS, UK*

[c] *ISIS Facility, Rutherford Appleton Laboratory, Harwell Oxford, Didcot, OX11 0QX, UK*

j.w.g.bos@hw.ac.uk

Half-Heuslers (HHs) are attracting widespread interest for thermoelectric waste heat recovery. This manuscript extends the known TiCoSb based HH compositions and provides new insight into their high-temperature stability. X-ray powder diffraction revealed an upper solubility limit near x = 0.4 for the $Ti_{1-x}V_xCoSb_{1-x}Sn_x$ series. Rietveld analysis of neutron powder diffraction data indicated that TiCoSb is stoichiometric, and confirmed that V and Sn are successfully co-substituted. Scanning electron microscopy revealed small grain sizes (< 5 μm) with up to 10-15% Ta along the boundaries due to reaction with the sample containment material. Repeated measurement of the electrical resistivity (ρ) and Seebeck coefficient (S) in a He atmosphere demonstrated that TiCoSb degrades rapidly at elevated temperatures. Scanning electron microscopy and X-ray diffraction reveal the formation of amorphous TiO_2 and crystalline CoSb, suggesting that the degradation is driven by exposure to trace amounts of oxygen. The unintentional incorporation of Ta leads to n-type doping and maximum power factors $S^2/\rho = 0.55$ mW m^{-1} K^{-2} at 550 K and $S^2/\rho = 0.8$ mW m^{-1} K^{-2} at 900 K were observed for TiCoSb and the x = 0.3 sample, respectively.

Introduction

The widespread implementation of thermoelectric generators has been limited by the lack of cost effective materials.[1] This has led to an ongoing research effort to find efficient, low cost, and environmentally friendly thermoelectric materials.[2, 3] The efficiency of a thermoelectric material is given by the figure of merit, $zT = (S^2/\rho\kappa)T$, where S is the Seebeck coefficient, ρ the electrical resistivity, κ is the sum of the lattice (κ_{lat}) and electronic (κ_{el}) thermal conductivities, and T is the absolute temperature. Half-Heuslers (HHs) have attracted extensive interest for thermoelectric applications due to their naturally large S and low ρ but are usually limited by large κ values.[4-7] The most heavily investigated compositions are p-type XCoSb and n-type XNiSn with X = Ti, Zr, Hf.[6, 7] The HH crystal structure consists of a face centred cubic lattice of a main group element (Z) with the X metals occupying the octahedral sites, and the late transition metals (Y) in half the available tetrahedral sites. The Y and Z elements therefore make up a zincblende substructure, which is semiconducting for 18 valence electrons.[4] Filling of all the tetrahedral sites results in a XY_2Z full-Heusler (FH) structure. It is well established that the properties of XNiSn HH materials are sensitive to sample processing, which can strongly affect the chemical composition and microstructure.[7] For example, TiNiSn can spontaneously form with excess Ni which segregates into $TiNi_2Sn$ domains,[8, 9] resulting in a reduced κ_{lat}.[10] Here, we present an investigation into the structure and properties of the $Ti_{1-x}V_xCoSb_{1-x}Sn_x$ solid solution, which connects the 18 electron HH compounds: TiCoSb and VCoSn. The latter has been subject to theoretical investigation[11-13] but has not been convincingly isolated.[14] It is unclear from the literature if TiCoSb is prone to similar spontaneous phase segregation into HH and FH phases. The absence of a FH $TiCo_2Sb$ phase suggests that this route for phase segregation may not be available. In addition, the reported thermoelectric data on TiCoSb are similar in many instances,[15-27] suggesting that this composition is indeed less susceptible to non-stoichiometry. To address the issue of phase segregation we have used neutron powder diffraction (NPD) and scanning electron microscopy (SEM) to determine the experimental compositions of the $Ti_{1-x}V_xCoSb_{1-x}Sn_x$ HH alloys. Another unresolved issue is the high-temperature stability of TiCoSb

based HHs. Typically, these phases show poorer thermal stability than TiNiSn based compounds.[19] A variable temperature synchrotron X-ray diffraction study of TiCoSb revealed the onset of sample degradation above 700 K, and the formation of metallic CoSb impurity phases.[28] No other impurity phases were observed in diffraction and it remains unclear what happens to Ti during sample decomposition. On the other hand, TiCoSb based samples show excellent cycling stability in vacuum with no discernible degradation of the thermoelectric properties even after 100s of temperature cycles.[29]

Experimental

A preliminary $Ti_{1-x}V_xCoSb_{1-x}Sn_x$ series (x = 0, 0.125, 0.25, 0.375, 0.5, 0.75 and 1) was synthesised to establish the solubility limit of VCoSn into TiCoSb. These samples were synthesised on a 1-gram scale via conventional solid-state reactions. Metal powders of Ti (-325 mesh, Alfa Aesar, 99.99%), V (-325 mesh, Alfa Aesar, 99.5%), Co (1.6 micron, Alfa Aesar, 99.8%), Sb (powdered shots, Alfa Aesar, 99.99%) and Sn (-100 mesh, Alfa Aesar, 99.85%) were used as starting materials. Stoichiometric amounts of the precursors were mixed using mortar and pestle, cold pressed into pellets and wrapped in Ta foil. The samples were sintered in evacuated sealed quartz tubes at 850 °C for 5 days with one intermediate homogenisation after 24 hours. Three 3 gram samples of TiCoSb and two 3 gram samples of $Ti_{0.7}V_{0.3}CoSb_{0.7}Sn_{0.3}$ were prepared in an identical manner and subsequently hot-pressed at 80 MPa and 850 °C for 20 minutes. The densities of the hot-pressed samples were determined using the Archimedes method and were >95% of the theoretical density. By contrast, the densities for the cold-pressed preliminary series were between 70-75% (Table S1 in the Electronic Supplementary Information). Laboratory X-ray powder diffraction data were collected from all samples on a Bruker D8 Advance diffractometer using Cu K_{a1} radiation over the range $10° \leq 2\theta \leq 120°$ for periods of time up to 8 hours. In addition, time-of-flight neutron powder diffraction data were collected from powdered pieces of hot-pressed TiCoSb and $Ti_{0.7}V_{0.3}CoSb_{0.7}Sn_{0.3}$ using the Polaris instrument at the ISIS pulsed spallation neutron source,

Rutherford Appleton Laboratory, UK, with data collection times of ~2-3 hours each. Phase identification and crystal structure refinement from the diffraction data (X-ray and neutron) was carried out by the Rietveld method using the GSAS and EXPGUI programs.[30, 31] The electrical resistivity and Seebeck coefficient were measured using a Linseis LSR-3 instrument. The chamber was evacuated down to 10^{-2} mbar, and purged with 99.996% He gas. The samples were taken out of the instrument between individual measurements. The microstructure and chemical composition of the hot-pressed TiCoSb and $Ti_{0.7}V_{0.3}CoSb_{0.7}Sn_{0.3}$ samples were analysed before and after the thermoelectric measurements using a Quanta 650 FEG scanning electron microscope. The working distance, operating voltage and spot size were 10 mm, 20kV and 4.5, respectively. Prior to analysis the samples were polished down to 0.5-micron roughness.

Results

Formation of the $Ti_{1-x}V_xCoSb_{1-x}Sn_x$ HH alloys: The X-ray powder diffraction patterns for the preliminary $Ti_{1-x}V_xCoSb_{1-x}Sn_x$ series are shown in Fig. 1. For $0 \leq x \leq 0.5$, the major reflections are matched with those for a cubic HH phase. For x = 0.625, 0.75, the patterns contained a mix of HH, FH and impurity peaks. For x = 1, the main peaks were indexed to a FH structure while a minor $CoSn_2$ phase was also unambiguously identified. It proved impossible to index the remaining reflections on any elemental or binary phases contained within the ICSD database. Significantly, the x = 1 sample was clearly free of any HH phase (Fig. 1). The lattice parameters were obtained from Rietveld fits and a = 5.8830(1) Å was obtained for TiCoSb, which is in excellent agreement with a = 5.8835(1) Å from synchrotron X-ray diffraction.[28] The composition dependence of the HH and FH lattice parameters are shown in Fig. 2. The HH lattice parameter shows a linear decrease to x = 0.43, beyond which no further change is observed. This suggests the formation of a solid solution with an upper limit near x = 0.43. The decrease in lattice parameter is consistent with the simultaneous replacement of Ti (1.47 Å) by V (1.35 Å) and Sn (1.58 Å) by Sb (1.59 Å). The FH lattice parameter has a more complex composition dependence with a minimum near x = 0.65 and

values between 5.9981(7) Å and 6.0129(2) Å (Fig. 2). This demonstrates that the FH composition changes but this is not clearly correlated with the nominal composition, which is in keeping with the observation of other intermetallic phases. The reported lattice parameters for VCo_2Sn in the ICSD database fall between 5.96-5.99 Å, which is significantly smaller than the values observed here. This suggests that our samples are somewhat V or Sn rich.

Structure of hot-pressed TiCoSb and $Ti_{1-x}V_xCoSb_{1-x}Sn_x$: The lattice parameters and density of the hot-pressed samples are summarised in Table 1, and representative X-ray diffraction patterns are shown in Fig. 3. The TiCoSb samples do not contain impurities, while a trace amount of FH phase was detected in the $Ti_{0.7}V_{0.3}CoSb_{0.7}Sn_{0.3}$ samples. Careful inspection of the X-ray patterns revealed a shoulder to the HH reflections for the x = 0.3 sample, and a broadened base for TiCoSb. This is illustrated by the close-up of the (420) reflection shown in the insets to Fig. 3. To further investigate the sample homogeneity SEM-EDX analysis was performed on the hot-pressed samples. The results are summarised in Fig. 4. The surfaces contain some small voids after polishing, and are characterised by average grain sizes <5 μm. No obvious segregation of any elements was observed but clear variations in brightness are evident in the backscattered images. In particular, the boundaries of the grains appear brighter, consistent with a higher average atomic number. Elemental analysis revealed that the variations in brightness are due to the presence of Ta which was used as the sample containment material. The compositions of the mapped areas in the TiCoSb sample are TiCoSb (I) and $Ti_{0.95}Ta_{0.05}CoSb$ (II), respectively. Three regions with varying Ta-concentration were observed in the x = 0.3 sample. These are $Ti_{0.81}V_{0.19}CoSb_{0.83}Sn_{0.17}$ (I), $Ti_{0.66}Ta_{0.1}V_{0.24}CoSb_{0.77}Sn_{0.22}$ (II) and $Ti_{0.64}Ta_{0.14}V_{0.22}CoSb_{0.77}Sn_{0.23}$ (III). In both cases, the core of the grains does not contain Ta, while the boundaries contain up to 10-15%. The inhomogeneous distribution suggests that the HH phase reacts slowly to the Ta foil after forming from the elemental precursors. Neutron powder diffraction was used to investigate the distribution of the metals over the available crystallographic sites. Neutron are suited to this because of the good neutron scattering contrast between the elements present: Ti (-3.44 fm), V (-0.38 fm), Co (2.49 fm), Sb (5.57 fm), Sn

(6.22 fm) and Ta (6.91 fm). The refined atomic parameters and fit statistics for the three investigated TiCoSb and one x = 0.3 composition are listed in Table 2, and the fit quality is illustrated in Fig. 5. For TiCoSb, initial fits revealed an improvement in χ^2 by increasing the average scattering strength on the Ti site. Substitution of 2-3% Ta for Ti led to significantly improved χ^2 values (typical $\Delta\chi^2$ = 0.2-0.3). Allowing for the partial occupancy of the vacant tetrahedral (Y2) site that becomes filled in case of a phase segregation into HH and nano-FH phases[8] did not further improve χ^2, and led to zero site occupancies (Table 2). This suggests that TiCoSb does not have the tendency to spontaneously form nanosegregated $TiCo_2Sb$ regions, as observed in the Ni-based half-Heuslers.[8, 10] However, we note that it is difficult to obtain unambiguous site occupancy information in these high-symmetry systems, and identical χ^2 values are possible for 10% Co occupancy of the Y2 site in the absence of Ta on the Ti site. The SEM-EDX data point towards the presence of Ta within the HH structure, and the best interpretation of the available data is therefore that there is no spontaneous segregation into HH and nano-FH phases. Inspection of the data for the x = 0.3 sample revealed the presence of shoulder to most but not all of the HH reflections. These were indexed on a FH phase with a = 5.9195(4) Å and a refined composition of $Co_{0.81(2)}Ti_{0.19(2)}(Co_{0.91(1)}Ti_{0.09(1)})_2Sb$ and an abundance of 9.1(1) wt%. Refinement of the site occupancies of the main HH phase, yielded a $Ti_{0.73(1)}V_{0.27(1)}Ta_{0.025}CoSb_{0.7}Sn_{0.3}$ composition, where the Sb and Sn ratio was kept fixed due to the small difference in neutron scattering length, and a similar amount of Ta substitution as in TiCoSb was assumed (Table 2). This confirms the successful double substitution of V and Sn in TiCoSb, which is also evident from the SEM-EDX analysis above. A second smaller 2.5(1) wt% FH VCo_2Sn phase with a larger lattice parameter, a = 6.0281(6) Å was also observed.

Thermoelectric power factor of TiCoSb: The temperature dependence of the electrical resistivity (ρ), Seebeck coefficient (S) and power factor (S^2/ρ) for the three hot-pressed TiCoSb samples (A, B, and C) are shown in Fig. 6. These samples were prepared under identical conditions and similar thermoelectric properties are observed. The ρ(T) curves show a metal-like temperature dependence

with $\rho_{300\ K}$ = 16-25 mΩ cm and $\rho_{723\ K}$ = 23-32 mΩ cm (Fig. 6a). The observation of degenerate rather than conventional semiconducting behaviour is consistent with n-type doping due to the incorporation of Ta. The S(T) is found to increase linearly from $S_{300\ K}$ = -250-300 μV K^{-1} to maximum values -330-370 μV K^{-1} at 600-700 K (Fig. 6b). The thermal bandgap was estimated using $E_g = 2|S_{max}|T_{max}$, yielding values of 0.48 eV (A), 0.40 eV (B) and 0.46 eV (C).[32] The samples attained similar maximum power factors S^2/ρ = 0.47 mW m^{-1} K^{-2} at 500 K (A), and 0.55 mW m^{-1} K^{-2} at 550 K (B and C, Fig 6c). Zhou et al have reported $\rho_{300\ K}$ = 20 mΩ cm, $S_{300\ K}$ = -210 μV K^{-1} and $(S^2/\rho)_{max}$ = 0.7 mW m^{-1} K^{-2} for 1% Ta substitution in TiCoSb.[23] These values are similar to our data and suggest that our samples contain ~1% Ta, which is in keeping with the compositions obtained from the Rietveld analysis.

Temperature stability of TiCoSb and $Ti_{0.7}V_{0.3}CoSb_{0.7}Sn_{0.3}$: To test the thermal stability of the materials, S and ρ measurements were performed on the hot-pressed samples under He atmosphere. The results of these repeat measurements are shown in Fig. 7. The ρ(T) for TiCoSb (sample B) shows a gradual decrease in magnitude for the measurements up to 723 K (B1-4, Fig. 7a). A sudden drop is observed at 723 K for run B5 that extends to 823 K and further reductions in magnitude are observed for run B6 (also up to 823 K, Fig. 7a). The S(T) show a gradual reduction in magnitude (Fig. 7b). The S^2/ρ improves up to a maximum of 0.9 mW m^{-1} K^{-2} at 575 K for run B5, and then decreases for run B6 (Fig. 7c). Post measurement X-ray powder diffraction revealed the presence of a 1-2 wt% metallic CoSb impurity. An identical experiment on a cold-pressed TiCoSb sample (~70% dense) from the preliminary series resulted in even more dramatic changes in the thermoelectric properties (Fig. S2 of the ESI). For this porous sample ~10 wt% CoSb after 6 repeats was observed (see Fig. S1 in the ESI). The lattice parameter of TiCoSb remained almost unchanged, demonstrating that its composition does not change. The hot-pressed x = 0.3 sample does not show the same dramatic changes in thermoelectric transport upon cycling (Fig. 7d-f). An initial drop in ρ is observed between measurement 1 and 2 but after that identical ρ(T) are observed up to 923 K (Fig. 7d). Similarly, the S(T) below 600 K for runs 2-4 are identical within the experimental error

(Fig. 7e). Above 650 K some discrepancies are observed, for example run A2 and A4 have S-shaped anomalies near 800 K, while run A3 is much smoother. The cause of the S-shaped response at high temperature is not clear but suggests that the sample is out of equilibrium. The relatively low ρ and high S values lead to power factors $S^2/\rho = 0.8$ mW m^{-1} K^{-2} at 923 K for the first measurement, and improving up to 1.2 mW m^{-1} K^{-2} for run 3 and 4 (Fig. 7f). Post measurement X-ray diffraction did not reveal the emergence of any clear impurities (Fig. S1 in the ESI). By contrast, the cold-pressed x = 0.375 sample shows evidence for degradation with the emergence of substantial CoSb and $CoSn_2$ impurity phases (Fig. S1 in the ESI). Interestingly, the thermoelectric properties of the cold-pressed V and Sn co-doped sample hold up much better compared to TiCoSb, despite the emergence of significant amounts of impurity phases (Fig. S2 in the ESI). To further investigate this degradation, we undertook SEM-EDX analysis on a polished piece of the dense TiCoSb sample used for the repeated cycling (sample B). Secondary electron (SE), backscattered electron (BSE) images and elemental maps for a representative area are shown in Fig. 8. Two distinct regions are evident in these images: on the left there is a large smooth area with EDX composition close to TiCoSb and towards the right contrast variations are evident. The elemental maps show the presence of substantial quantities of oxygen at the right part of the image, while the left side is nearly free of oxygen. The SE image reveals that the inhomogeneous area on the right is relatively smooth and confirms that the BSE contrast variations are due to compositional variations. EDX analysis yields compositions consistent with TiO_2 and CoSb. The microscopy therefore demonstrates that TiCoSb decomposes into TiO_2 and CoSb. The morphology of the oxidised areas and the absence of TiO_2 in the X-ray powder diffraction data demonstrates that this is an amorphous phase.

Discussion

An upper solubility limit near x = 0.4 was established for the $Ti_{1-x}V_xCoSb_{1-x}Sn_x$ HH alloys, demonstrating that VCoSn cannot be prepared. This observation is in agreement with a recent

computational study that predicted that VCoSn is unstable due to the formation of competing phases,[33] which is in keeping with our diffraction data, although we could not unambiguously index all phases present (Fig. 1). Analysis of the experimental compositions of the $Ti_{1-x}V_xCoSb_{1-x}Sn_x$ solid solution using NPD and SEM demonstrates that TiCoSb is stoichiometric, except for the incorporation of Ta along the grain edges due to reaction to the sample containment material. TiCoSb therefore does not appear to be as susceptible to non-stoichiometry as TiNiSn.[8, 9] This may be related to the absence of a $TiCo_2Sb$ FH phase or the absence of other competing phases as calculated for TiNiSn.[34] The thermoelectric properties for the repeat TiCoSb (samples A-C) and x = 0.3 samples (sample A, B) are similar (Figs. 6, 7) showing that the synthesis protocol leads to reproducible results. Maximum power factors $S^2/\rho = 0.5$ mW m^{-1} K^{-2} (x = 0) and $S^2/\rho = 0.8$ mW m^{-1} K^{-2} (x = 0.3) are observed. Both TiCoSb and $Ti_{1-x}V_xCoSb_{1-x}Sn_x$ show degradation after repeated measurements of their thermoelectric properties in a He atmosphere. The observed changes are more pronounced for TiCoSb than for the V and Sn substituted samples. However, post measurement analysis reveals the formation of significant amounts of CoSb (and $CoSn_2$) in all cases, in particular for the porous cold-pressed samples. This immediately suggest a link to the presence of trace amounts of atmospheric oxygen. The SEM and elemental analysis confirms the presence of amorphous TiO_2. A back of the envelope calculation suggests that ~2% of TiCoSb can be converted to TiO_2 and CoSb in each measurement before depleting the oxygen present in the measurement chamber. The observation of ~10 wt% CoSb for the porous samples after 6 repeats is therefore feasible, and consistent with our experimental data. Further indirect support for the oxidation of Ti as the driving force for the degradation comes from the analogous XCoSb phases with Zr and Hf which have been measured up to 800-900 °C in a similar atmosphere without any reported degradation.[35] Excluding oxygen also leads to improved stabilities as evidenced by the recent report of up 100s of heating cycles in vacuum without any degradation in properties.[29] The similar lattice parameters for the HH phases before and after cycling suggests that the composition

of the HH phase itself does not change during measurement, and that the degradation in the thermoelectric properties is due to sample oxidation.

To summarise, TiCoSb forms as a stoichiometric phase and does not show the same tendency to spontaneously phase segregate into HH and nano-FH phases that is observed for TiNiSn. The $Ti_{1-x}V_xCoSb_{1-x}Sn_x$ HH alloys can be prepared up to x = 0.4 and are reactive towards oxygen at moderate temperatures with the formation of amorphous TiO_2 and crystalline CoSb and $CoSn_2$ phases evident from post measurement analysis. This demonstrates that thermoelectric generators based on these HH phases will need to be carefully encapsulated.

Acknowledgments

MA acknowledges the British Council for support.

Table 1. Overview of the lattice parameters (a), room temperature Seebeck coefficient (S), electrical resistivity (ρ), percentage density and estimated bandgap (see text) for the hot-pressed repeat samples of TiCoSb and $Ti_{0.7}V_{0.3}CoSb_{0.7}Sn_{0.3}$.

Composition	Sample	a (Å)	S (μV K^{-1})	ρ (mΩ cm)	Density (%)	E_g (eV)
TiCoSb	A	5.8830(1)	-305	25.5	95	0.46
	B	5.8829(1)	-298	23.7	97	0.40
	C	5.8831(1)	-251	16.2	98	0.48
$Ti_{0.7}V_{0.3}CoSb_{0.7}Sn_{0.3}$	A	5.8737(1)	-85	2.7	100	-
	B	5.8714(1)	-95	2.9	97	-

Table 2. Structural parameters and fit statistics for TiCoSb (samples A-C) and $Ti_{0.7}V_{0.3}CoSb_{0.7}Sn_{0.3}$ (sample A) obtained from Rietveld fits against Polaris neutron powder diffraction data.

		TiCoSb (A)	TiCoSb (B)	TiCoSb (C)	$Ti_{0.7}V_{0.3}CoSb_{0.7}Sn_{0.3}$ (A)
a (Å)		5.8858(1)	5.8819(1)	5.8830(1)	5.8737(1)
X	U_{iso} ($Å^2$)	0.0039(1)	0.0040(1)	0.0039(1)	0.0047(1)
	Occ	$Ti_{0.98(1)}Ta_{0.02(1)}$	$Ti_{0.98(1)}Ta_{0.02(1)}$	$Ti_{0.97(1)}Ta_{0.03(1)}$	$Ti_{0.70(1)}V_{0.27(1)}Ta_{0.025}$
Y1	U_{iso} ($Å^2$)	0.0039(1)	0.0040(1)	0.0039(1)	0.0077(1)
	Occ	Co	Co	Co	Co
Y2	U_{iso} ($Å^2$)	0.0039(1)	0.0040(1)	0.0039(1)	-
	Occ	$Co_{0.001(4)}$	$Co_{0.002(3)}$	$Co_{0.001(3)}$	-
Z	U_{iso} ($Å^2$)	0.0039(1)	0.0040(1)	0.0039(1)	0.0039(1)
	Occ	Sb	Sb	Sb	$Sb_{0.7}Sn_{0.3}$
χ^2		1.3	1.9	1.4	2.0
Bank5	wR_p (%)	2.1	2.6	1.5	2.5
	R_p (%)	3.7	3.6	2.5	4.0
Bank4	wR_p (%)	1.8	1.7	1.6	1.7
	R_p (%)	3.7	4.0	3.5	2.8
Bank3	wR_p (%)	2.0	2.4	1.9	3.2
	R_p (%)	6.8	3.0	2.5	7.4

The $Ti_{0.7}V_{0.3}CoSb_{0.7}Sn_{0.3}$ sample contained 9.1(1) wt% of a full-Heusler phase with refined composition $Co_{0.81(2)}Ti_{0.19(2)}(Co_{0.91(1)}Ti_{0.09(1)})_2Sb$ (a = 5.9195(4) Å) and 2.5(1) wt% of VCo_2Sn (a = 6.0281(6) Å). HH phases; X: 4a (0, 0, 0); Y1: 4c (¼, ¼, ¼); Y2: 4d (¾, ¾, ¾); Z 4b (½, ½, ½).

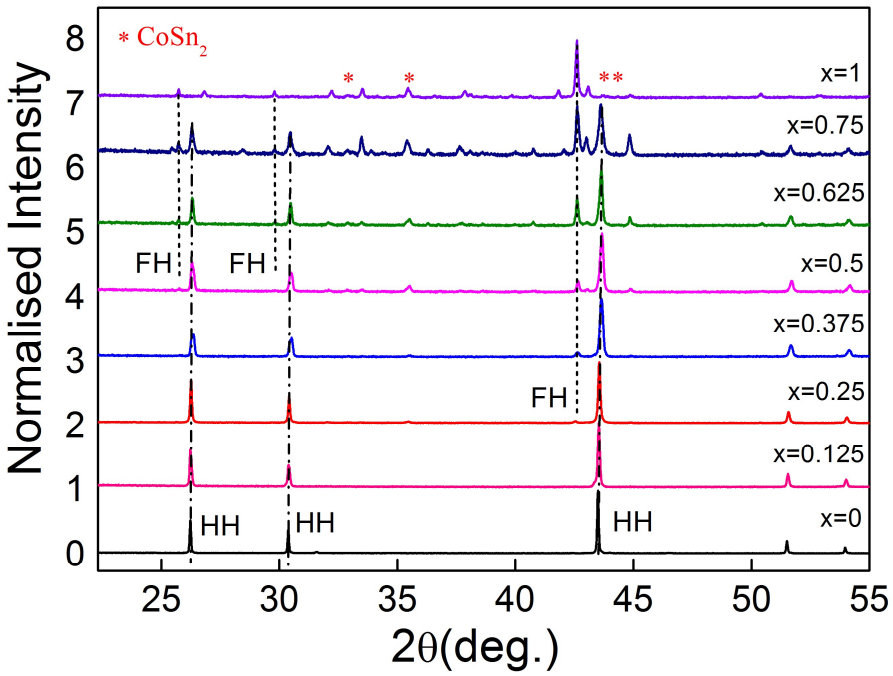

Figure 1. X-ray powder diffraction patterns for the $Ti_{1-x}V_xCoSb_{1-x}Sn_x$ series. Data have been normalised and offset by 1. The x = 0 sample is phase pure TiCoSb (HH), while the dominant peaks for x = 1 correspond to a full-Heusler (FH) phase (VCo_2Sn). The unindexed reflections for $x \geq 0.5$ do not correspond to any known phases contained within the ICSD database.

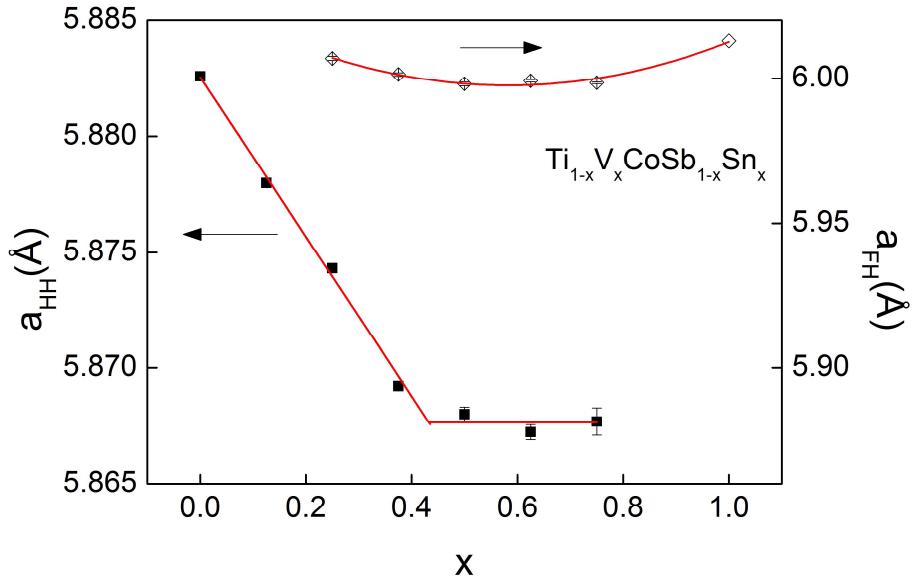

Figure 2. Composition dependence of the half-Heusler (a_{HH}) and full-Heusler (a_{FH}) lattice parameters for the $Ti_{1-x}V_xCoSb_{1-x}Sn_x$ series.

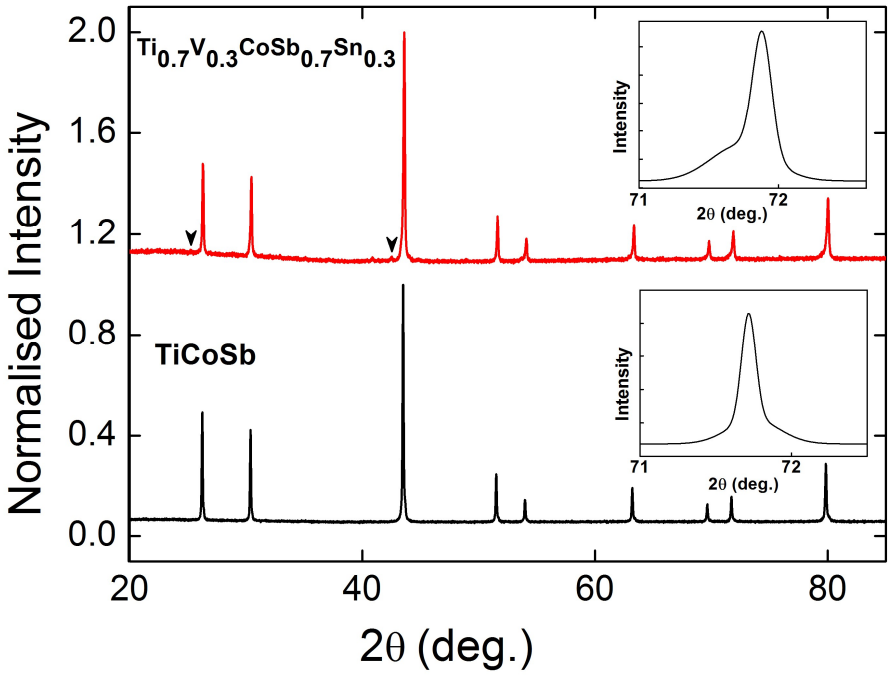

Figure 3. X-ray powder diffraction patterns for TiCoSb and $Ti_{0.7}V_{0.3}CoSb_{0.7}Sn_{0.3}$. The insets illustrate the broadening of the half-Heusler reflections. (Data have been normalised and offset by 1; ▼: VCo_2Sn).

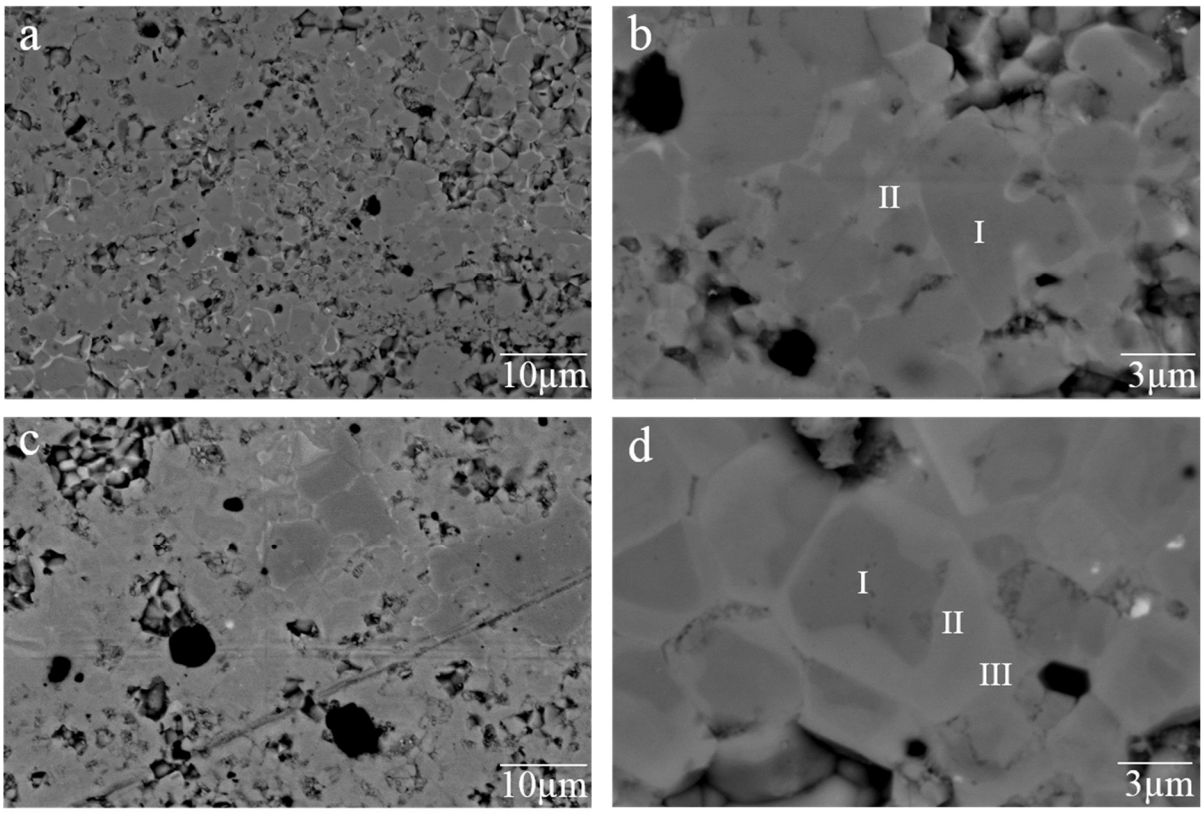

Figure 4. Backscattered electron SEM images for TiCoSb (a, b) and $Ti_{0.7}V_{0.3}CoSb_{0.7}Sn_{0.3}$ (c, d). These images reveal relatively small grains and show evidence for reaction to Ta at the grain boundaries. For TiCoSb, the compositions of regions I and II are TiCoSb and $Ti_{0.95}Ta_{0.05}CoSb$. The compositions for $Ti_{0.7}V_{0.3}CoSb_{0.7}Sn_{0.3}$ are I: $Ti_{0.81}V_{0.19}CoSb_{0.83}Sn_{0.17}$; II: $Ti_{0.66}Ta_{0.1}V_{0.24}CoSb_{0.77}Sn_{0.22}$ and III: $Ti_{0.64}Ta_{0.14}V_{0.22}CoSb_{0.77}Sn_{0.23}$. The inhomogeneous distribution of Ta suggests a slow reaction to the sample containment material, which is in keeping with its high melting point (3020 °C).

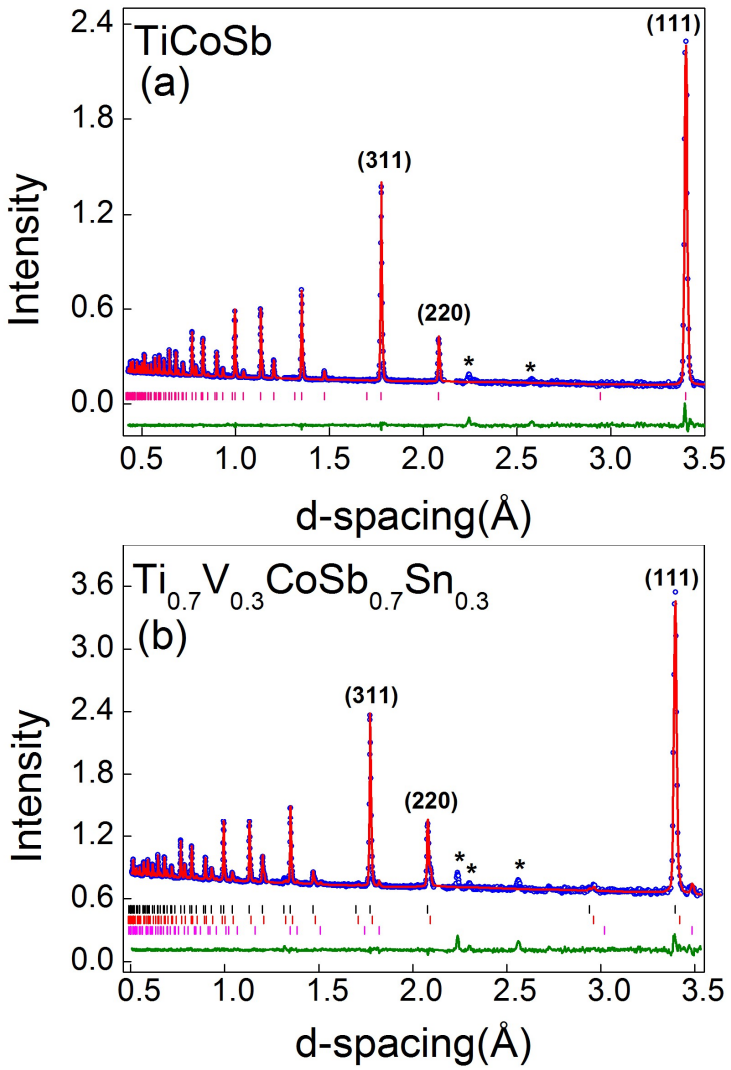

Figure 5. Rietveld fit to Polaris neutron powder diffraction data for TiCoSb and $Ti_{0.7}V_{0.3}CoSb_{0.7}Sn_{0.3}$. In (a) the reflection markers are for TiCoSb. In (b) the top, middle and bottom markers are for $Ti_{0.7}V_{0.3}CoSb_{0.7}Sn_{0.3}$, $Co_{0.81(2)}Ti_{0.19(2)}(Co_{0.91(1)}Ti_{0.09(1)})_2Sb$ and VCo_2Sn. An unindexed impurity phase labelled by asterisks is observed in both samples. Data shown are from detector bank 4.

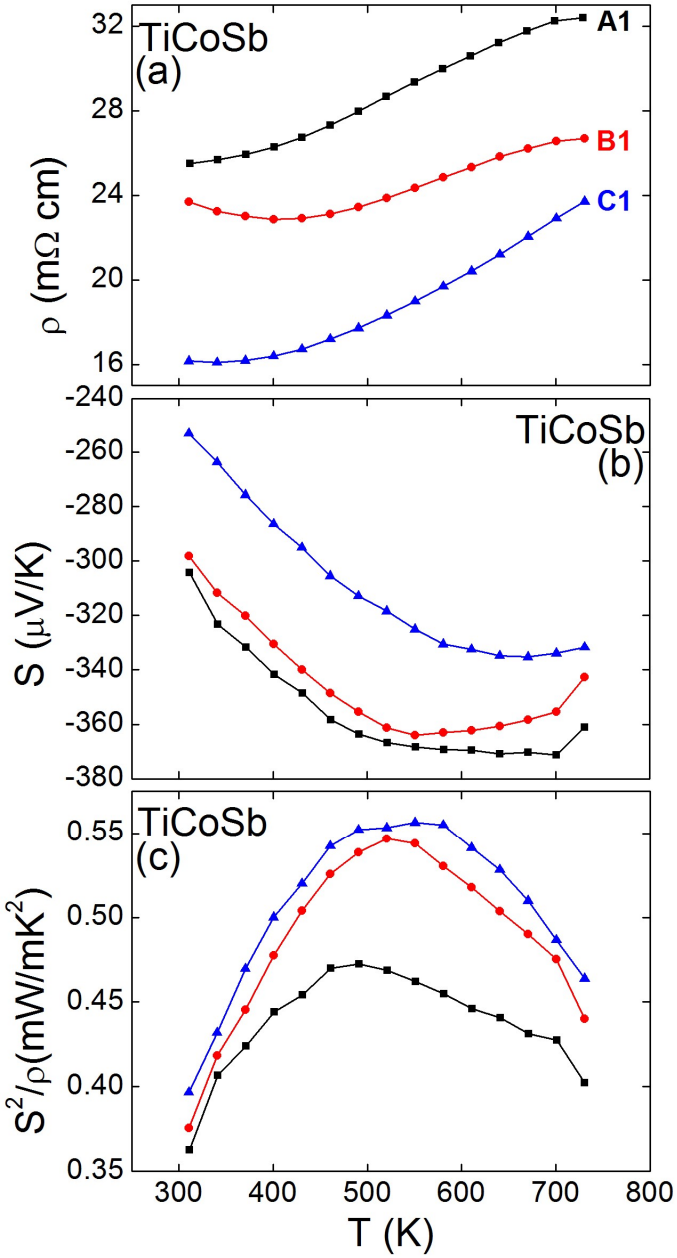

Figure 6. Temperature dependence of the electrical resistivity (ρ), Seebeck coefficient (S), and thermoelectric power factor (S^2/ρ) for the three hot-pressed TiCoSb samples (first measurement).

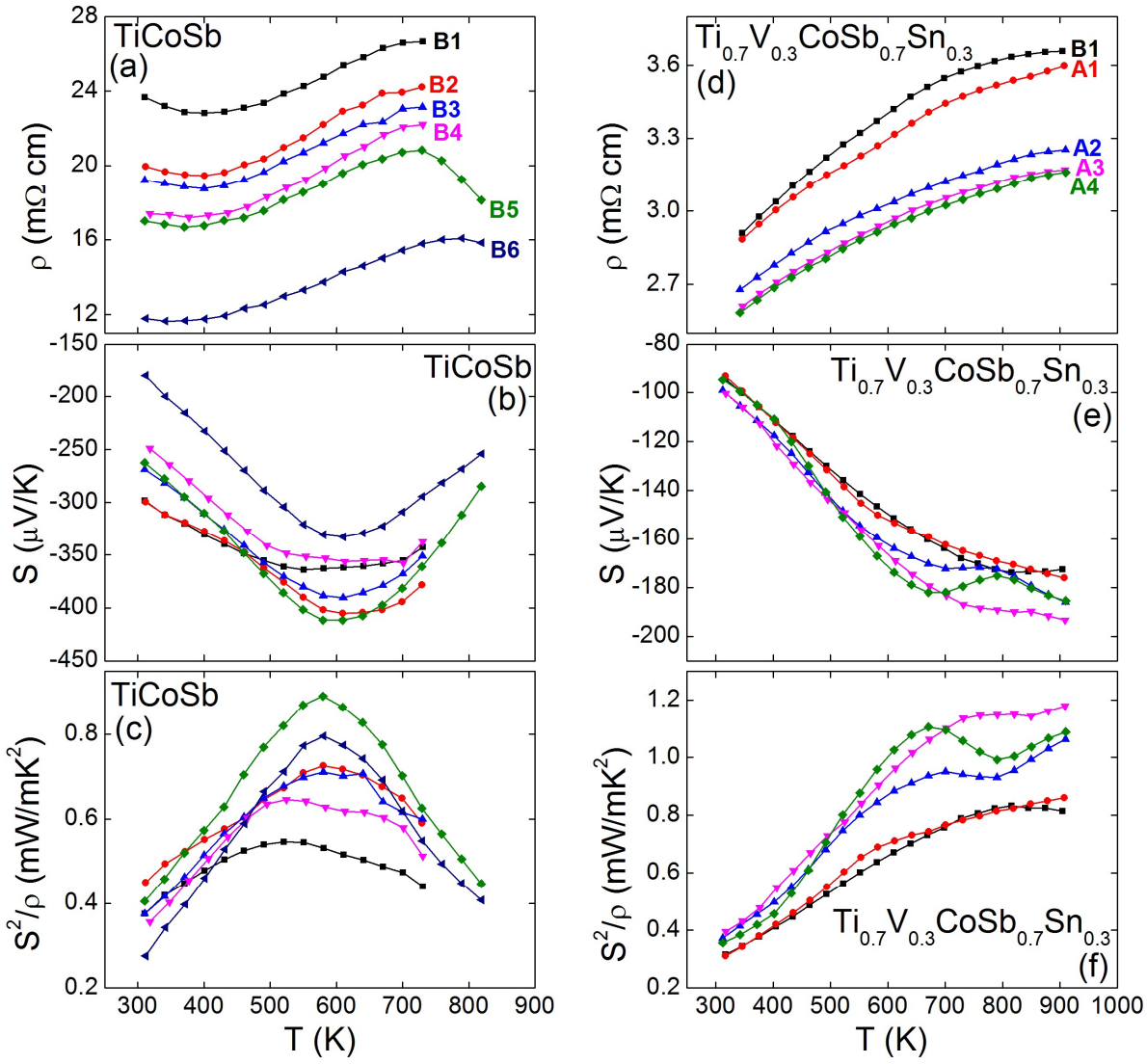

Figure 7. Repeatability testing of the electrical resistivity (ρ), Seebeck coefficient (S), and thermoelectric power factor (S^2/ρ) of TiCoSb and $Ti_{0.625}V_{0.375}CoSb_{0.625}Sn_{0.375}$. Measurements shown were undertaken on sample B for TiCoSb and samples A and B for $Ti_{0.625}V_{0.375}CoSb_{0.625}Sn_{0.375}$. The following sequence was used for TiCoSb: 4 consecutive measurements up to 723 K (B1-4); followed by 2 measurements up to 823 K (B5-6). For $Ti_{0.625}V_{0.375}CoSb_{0.625}Sn_{0.375}$, 4 consecutive measurements up to 923 K are shown for sample A (A1-4) and the first measurement is shown for sample B (B1). The samples were taken out of the instrument between individual measurements.

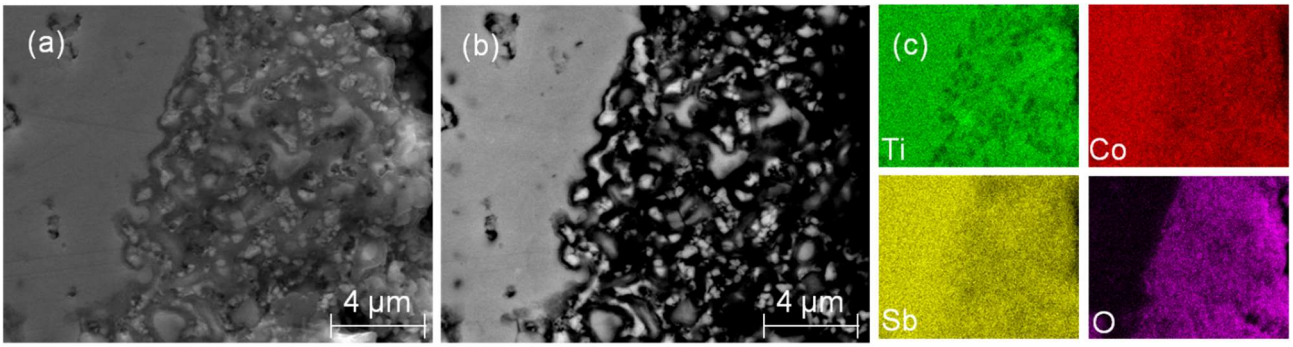

Figure 8. (a) Secondary electron, (b) back scattered scanning electron microscopy images and (c) elemental maps for the hot-pressed TiCoSb sample B after repeated measurement of the thermoelectric properties (see Fig. 7 for property data).

References

1. D. M. Rowe, ed., *Thermoelectrics and its Energy Harvesting*, CRC Press Boca Raton, 2012.
2. G. J. Snyder and E. S. Toberer, *Nature materials*, 2008, **7**, 105-114.
3. J. R. Sootsman, D. Y. Chung and M. G. Kanatzidis, *Angewandte Chemie International Edition*, 2009, **48**, 8616-8639.
4. T. Graf, C. Felser and S. S. P. Parkin, *Progress in Solid State Chemistry*, 2011, **39**, 1-50.
5. W. J. Xie, A. Weidenkaff, X. F. Tang, Q. J. Zhang, J. Poon and T. M. Tritt, *Nanomaterials*, 2012, **2**, 379-412.
6. S. Chen and Z. F. Ren, *Materials Today*, 2013, **16**, 387-395.
7. J. W. G. Bos and R. A. Downie, *Journal of Physics-Condensed Matter*, 2014, **26**, 433201.
8. R. A. Downie, R. I. Smith, D. A. MacLaren and J. W. G. Bos, *Chemistry of Materials*, 2015, **27**, 2449-2459.
9. R. A. Downie, S. A. Barczak, R. I. Smith and J. W. G. Bos, *Journal of Materials Chemistry C*, 2015, **3**, 10534-10542.
10. R. A. Downie, D. A. MacLaren, R. I. Smith and J. W. G. Bos, *Chemical communications*, 2013, **49**, 4184-4186.
11. S. Ogut and K. M. Rabe, *Physical Review B*, 1995, **51**, 10443-10453.
12. M. Hichour, D. Rached, R. Khenata, M. Rabah, M. Merabet, A. H. Reshak, S. Bin Omran and R. Ahmed, *Journal of Physics and Chemistry of Solids*, 2012, **73**, 975-981.
13. M. Ameri, A. Touia, R. Khenata, Y. Al-Douri and H. Baltache, *Optik - International Journal for Light and Electron Optics*, 2013, **124**, 570-574.
14. C. S. Lue, Y. Oner, D. G. Naugle and J. H. Ross, *Ieee T Magn*, 2001, **37**, 2138-2140.
15. Y. Xia, V. Ponnambalam, S. Bhattacharya, A. L. Pope, S. J. Poon and T. M. Tritt, *Journal of Physics-Condensed Matter*, 2001, **13**, 77-89.
16. Y. Kawaharada, K. Kurosaki, H. Muta, M. Uno and S. Yamanaka, *Journal of Alloys and Compounds*, 2004, **384**, 308-311.
17. M. Zhou, L. D. Chen, W. Q. Zhang and C. D. Feng, *Journal of Applied Physics*, 2005, **98**, 013708.
18. M. Zhou, C. D. Feng, L. D. Chen and X. Y. Huang, *Journal of Alloys and Compounds*, 2005, **391**, 194-197.
19. T. Sekimoto, K. Kurosaki, H. Muta and S. Yamanaka, *Journal of Alloys and Compounds*, 2005, **394**, 122-125.
20. T. Sekimoto, K. Kurosaki, H. Muta and S. Yamanaka, *Materials Transactions*, 2005, **46**, 1481-1484.
21. T. Sekimoto, K. Kurosaki, H. Muta and S. Yamanaka, *Journal of Alloys and Compounds*, 2006, **407**, 326-329.
22. T. Wu, W. Jiang, X. O. Li, Y. F. Zhou and L. D. Chen, *Journal of Applied Physics*, 2007, **102**, 103705.
23. M. Zhou, L. D. Chen, C. D. Feng, D. L. Wang and J. F. Li, *Journal of Applied Physics*, 2007, **101**, 113714.
24. T. Wu, W. Jiang, X. Y. Li, S. Q. Bai, S. C. Liufu and L. D. Chen, *Journal of Alloys and Compounds*, 2009, **467**, 590-594.
25. J. Barth, B. Balke, G. H. Fecher, H. Stryhanyuk, A. Gloskovskii, S. Naghavi and C. Felser, *Journal of Physics D-Applied Physics*, 2009, **42**, 185401.
26. P. Qiu, X. Huang, X. Chen and L. Chen, *Journal of Applied Physics*, 2009, **106**, 103703.
27. S. Ouardi, G. H. Fecher, C. Felser, M. Schwall, S. S. Naghavi, A. Gloskovskii, B. Balke, J. Hamrle, K. Postava, J. Pištora, S. Ueda and K. Kobayashi, *Physical Review B*, 2012, **86**, 045116.
28. I. Skovsen, L. Bjerg, M. Christensen, E. Nishibori, B. Balke, C. Felser and B. B. Iversen, *Dalton transactions*, 2010, **39**, 10154-10159.
29. E. Rausch, B. Balke, S. Ouardi and C. Felser, *Energy Technology*, 2015, **3**, 1217-1224.

30. A. C. Larson and R. B. Von Dreele, in *Los Alamos National Laboratory Report LAUR*, 2000, pp. 86-748.
31. B. H. Toby, *Journal of Applied Crystallography*, 2001, **34**, 210-213.
32. H. J. Goldsmid and J. W. Sharp, *Journal of Electronic Materials*, 1999, **28**, 869-872.
33. R. Gautier, X. W. Zhang, L. H. Hu, L. P. Yu, Y. Y. Lin, T. O. L. Sunde, D. Chon, K. R. Poeppelmeier and A. Zunger, *Nature Chemistry*, 2015, **7**, 308-316.
34. J. E. Douglas, C. S. Birkel, N. Verma, V. M. Miller, M.-S. Miao, G. D. Stucky, T. M. Pollock and R. Seshadri, *Journal of Applied Physics*, 2014, **115**, 043720.
35. X. A. Yan, G. Joshi, W. S. Liu, Y. C. Lan, H. Wang, S. Lee, J. W. Simonson, S. J. Poon, T. M. Tritt, G. Chen and Z. F. Ren, *Nano Letters*, 2011, **11**, 556-560.